Cohesive strength and fracture toughness of atmospheric ice

V. Palanque[1,2*], E. Villeneuve[3*], M. Budinger[4], V. Pommier-Budinger[2] and G. Momen[3]

[1*]ISAE-SUPAERO, University of Toulouse, 10 Avenue Edouard Belin, Toulouse, 31400 France.
[2*]ONERA/MFE, University of Toulouse, F-31055, Toulouse France.
[3]AMIL, University of Quebec at Chicoutimi, 555 boulevard de l'Université, G7H 2B1,Chicoutimi, Quebec, Canada.
[4]Institut Clément Ader (ICA), University of Toulouse, INSA, ISAE-SUPAERO, MINES 9 ALBI, UPS, CNRS, 610101, France.

*Corresponding author(s). E-mail(s): valerian.palanque@isae-supaero.fr; eric.villeneuve@uqac.ca;
Contributing authors: mbudinge@insa-toulouse.fr; valerie.budinger@isae-supaero.fr; gelareh.momen@uqac.ca;

Abstract

This paper aims at defining key mechanical properties of atmospheric ice in order to improve the design of mechanical de-icing systems. Based on ice fracture mechanisms, the parameters of interest are the cohesive strength of the ice and its fracture toughness. An hybrid experimental/numerical vibrating method is used to measure those critical values. Parameters such as temperature and precipitation rate influence the ice density and ice samples are thus defined with respect to this parameter. First the cohesive strength of ice is measured over the entire range of ice density and a polynomial expression of the cohesive strength of ice is given as a function of this density. Then the fracture toughness is measured for a smaller range of density and an average critical value is given. Finally, the influence of the

properties computed are discussed to assess the conditions of atmospheric ice mechanical removal and the challenges for the design of mechanical ice protection systems. The study tends to show that as its density decreases, ice is more difficult to remove mechanically.

Keywords: Atmospheric ice, Tensile Strength, Fracture toughness, Density, Cold room, Experimental, Numerical model, Vibration test

1 Introduction

Atmospheric icing occurs when suspended droplets (in clouds) or precipitations droplets impinge on surfaces with surrounding temperature below the freezing point. In freezing environment, droplets become super-cooled, triggering the freezing process upon impact, leading to the atmospheric ice creation [1]. Because of its mass and volume, the adhered ice constitutes a major threat for the iced structures. For instance, telecommunication towers, electrical pylons and high voltage wires, are threatened with collapsing under their weight in poor weather conditions (e.g. 1998 ice storm in North America). In the case of airfoil structures, the accreted ice deteriorates the operation. For instance, wind turbines, rotor-blades and airfoil are impacted by having their aerodynamics properties altered [2–7]. In many industrial fields, such threats are not acceptable and therefore need to be resolved. Embedded mechanical de-icing systems are designed in order to remove the accreted ice [8–19]. The design of efficient mechanical de-icing systems is however conditioned by the knowledge of the ice mechanical properties. To achieve mechanical de-icing, the properties of interest are mainly the density, the Young's modulus, the cohesion strength, the adhesion strength and the fracture toughness.

The reference ice entity is the single crystal of ordinary Ice Ih. The mono crystal of ice Ih is by nature anisotropic and its properties were investigated by many

researchers as described in [20–22]. From its tetrahedral arrangement with oxygen atoms and water molecules separated by 2.76 Å, the pure mono crystal density of ice Ih is estimated to 917 kg/m^3 [22]. In 1940, Dorsey [23] gave a complete review of ice properties measured so far and the method used. However, in the case of atmospheric icing, the ice grows in a globally "isotropic" polycrystalline assembly [24]. Moreover, because of its granular constitution and the inherent existence of imperfection within the ice grain boundaries, the polycrystalline ice does not always follow standard elastic behavior. According to Hobbs [20], the elastic behavior of a crystal is due to changes in inter-molecular distances, nevertheless, the ice impurities favors inter-grain movement, triggering the non elastic behavior of the material. Applying reduced strain magnitude load for short periods allows to stay in the elastic domain. Gold [25] defined maximum values for load (0.1 MPa) and strain rate (5 kPa.s^{-1}) preventing from miss-measuring inter grain displacement as elastic strain. Low magnitude and high strain rate measurements allowed to approach Young's modulus value for poly-crystalline ice with accuracy [20, 26]. Schulson et.al [27] gave a standard value of 9.0 GPa for poly crystalline ice at -5°C and a 0.33 Poisson ratio. Various studies have shown that the loss of density i.e. the increase of the porosity of the ice led to a loss in the mechanical properties of the ice [28, 29]. In [30], Palanque et.al gave a concrete expression of the atmospheric ice Young's modulus according to the density. The decrease of the stiffness is explained by the presence of air bubbles, trapped in the freezing process replacing solid material. It was demonstrated that this ice property is highly correlated with the ice density, and that therefore, ice could be characterized by its density in a continuous manner, being much more accurate to describe the atmospheric ice than the standard ice type discretization. The influence of

the density of the sea ice on its mechanical properties was investigated in [31–33] showing that additionally to the loss of stiffness, the strength of the ice also tends to decrease with the density. The cohesive strength of the atmospheric ice was investigated by Druez et.al in [34, 35]. Ice was created thanks to an open wind tunnel for different temperatures, liquid water content (LWC) and wind speed. Standard static tests were performed to assess the strength of the material. According to Petrovic [36] the value for the tensile strength of the ice is in the [0.7 - 3.1] MPa range. Depending on the iced area configuration and the mechanical loading of the ice, the adhesiveness is either controlled by its adhesive shear strength or its interfacial toughness [37]. In 2018, Work [38] published a review of the measured adhesive properties of ice found in the literature. Among the studies, some focused on the adhesive shear strength of atmospheric ice [39–41] highlighting the difference in critical shear value for different ice types. Others [42–44] measured the fracture toughness of the ice using standard blister test for different substrate materials and temperature.

This paper proposes a hybrid numerical/experimental method to measure the cohesive strength and the fracture toughness of the atmospheric ice for a broad range of ice density accumulated at multiple different cold chamber icing conditions. As described in previous work [30], the ice "type" is defined by its density and thanks to the use of a hybrid numerical/experimental method based on vibration measurements, the accuracy of the results is increased [26]. The results from this study aims to provide accurate critical values of such properties for different types of ice characterized by their density in order to help the design of efficient mechanical de-icing systems.

First the fracture mechanics assumptions used to describe the crack initiation and propagation behavior are defined. The experimental set up and the numerical model used for the method are then described and the hybrid

method is detailed. The experimental results and the critical values of the cohesive strength and the fracture toughness obtained are given according to the density. Finally, the impact of the ice density on the de-icing requirement is discussed using the cohesive strength and the fracture toughness values given in this paper combined with the results from previous paper [30].

2 Method and Material

2.1 Mechanical de-icing mechanisms

The method used in this paper is a hybrid experimental/numerical finite element method based on mechanical fracture mechanisms. The objective is to identify the critical values involved in mechanical de-icing by comparing de-icing tests with finite element computations issued from high fidelity 3D models.

According to experimental configuration, various ice fracture mechanisms can be observed. Using a standard push test, [37, 45] researchers studied the adhesive debonding under interfacial shear stress loading. The debonding condition was observed to be mixed mode crack opening (energy release rate) at first and shear stress debonding (stress) finally. Ronneberg et .al [39] investigated adhesive shear strength of the ice using a spin test on short ice blocs. The configuration used in this study (described in figure 1) has been studied in previous works [12, 19, 46, 47]. The ice is accumulated on the sample covering the whole surface of the substrate. As the length of the deposit is greater than its thickness, the fracture mechanism under flexural load is known to be cohesive at first with the initiation of a crack in the ice bulk at the anti-node location, followed by an energy release rate adhesive fracture propagation, starting from the cohesive crack location. This setup therefore allows to study the cohesive strength and the fracture toughness of the ice.

2.2 Test samples definition

The samples used in this paper are the same as in [30]. To execute the method introduced in this paper, ice must be accreted to an elastic substrate to allow the loading. The thickness of the substrate and its material are chosen to fit with aerospace airfoil standards: an aluminum sample (1.5 mm-thick) and a titanium sample (1 mm-thick) are machined. The samples are equipped with two 1 mm-thick piezo-electric ceramics (PIC 181). Ceramics are placed in a symmetric way to ensure the double axis-symmetry of the whole sample (Figure 1). It is possible to use each of them either as a sensor or an actuator. The dimensions of the plate are chosen to match with results from Gold et.al study [26] in which the authors showed that, as the load rate increases, the scattering of the Young's modulus measurement decreases, reaching an horizontal asymptotic for load rates above 500 Hz. Hence, the size of the sample is reduced to increase the first mode frequency of the un-iced titanium sample just above 500 Hz, ensuring that the loading of the ice will occur at sufficient rate whatever the ice deposit is (has ice thickness increases the frequency of the mode).

A total of three titanium samples and one aluminum sample are machined. From the authors' experience, the titanium allows a better view of the adhesive crack due to the reflection of the material surface, which made the titanium sample the best candidate for being the reference sample. 3 samples were therefore machined to enable comparison of repeatability. Then, in order to observe the influence of the substrate's material, an Aluminum sample was machined. As the repeatability of the experiment could have already been confirmed on the titanium samples, multiplying the number of Aluminum

sample did not appear relevant. The samples dimensions are obtained accurately using a measuring column and are summarized in Table 1.

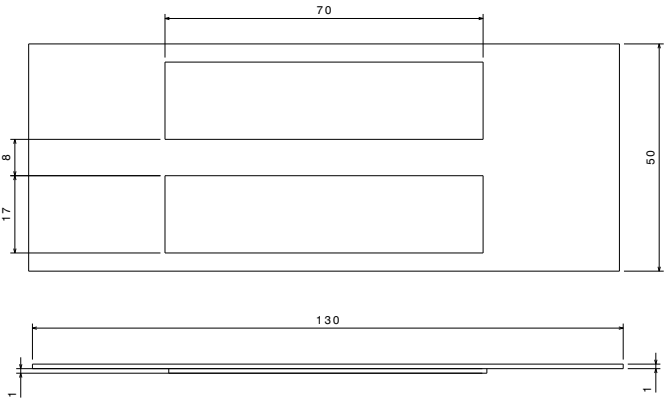

Fig. 1: Titanium substrate and ceramics configuration (in mm)

Table 1: Measurements of the four samples dimensions

	Sample 1	Sample 3	Sample 4	Sample Al
Material	Ti TA6V	Ti TA6V	Ti TA6V	Al 5754
Thickness(mm)	1.10 ±0.01	1.11±0.01	1.11±0.01	1.51±0.01
Width (mm)	49.48 ±0.15	49.68±0.01	49.80±0.10	49.32±0.20
Length(mm)	130.27 ±0.03	130.39±0.04	131.08±0.01	128.90±0.05

2.3 Condition for fracture initiation and propagation

2.3.1 Cohesive fracture initiation

In order to assess the cohesive strength of the ice, cohesive failure is obtained experimentally on the test sample. Experimental load conditions upon failure are retrieved and inputted in the FEM model and the stress field is retrieved from the computation. The critical strength is then assessed by identification of

the stress value when failure is initiated. However, the critical value identified directly depends on the chosen criterion to define the failure. It is therefore of utmost importance to define correctly the failure condition.

As commonly mentioned in the literature, ice is considered as a brittle material [20, 23, 36, 48]. Rankine theory defines the Maximum Stress Theory in which the initiation of crack in brittle material occurs when the principal stress σ_I exceeds the tensile strength of the material. A cohesive crack is initiated for $C_1 \geq 1$ (1) where C_1 is given by:

$$C_1 = \frac{\sigma_I}{\sigma_{adm}} \tag{1}$$

with σ_I the principal stress in the ice and σ_{adm} the tensile strength of the ice.

2.3.2 Fracture propagation

Similar to cohesive fracture, the adhesive crack propagation is first observed experimentally. The loading conditions and the corresponding crack lengths are retrieved and supplied to the FEM model.

As shown in [47], for the experimental set up used in this paper, the adhesive crack propagates in a energy release rate dominated mechanism. The global criterion used for this kind of brittle crack propagation is Griffith's criterion [49]. The crack propagation is assessed by comparing the energy release rate G to a critical value (interface fracture toughness) G_c. Griffith's theory defines that a crack propagates in the case of $C_2 \geq 1$ (2) where C_2 is given by:

$$C_2 = \frac{G}{G_c} \tag{2}$$

According to the loading conditions, the expression of the global energy release

rate G can be divided into three elementary crack opening modes. In the case of pure mode I opening, the crack propagates if the load is maintained above the critical value. The toughness of the material is therefore characterized by the mode I stress intensity factor K_{IC}. In the case of an interfacial crack between two different materials, the non homogeneity between the two edges of the crack often leads to a mixed mode loading of the crack tip [50]. Hence, a combination of normal (mode I) and shear (mode II and mode III) opening is observed. In the case of mixed mode opening, the following criterion is defined to assess the crack propagation (3) [51]:

$$\frac{G_I}{G_{Ic}} + \frac{G_{II}}{G_{IIc}} = 1 \tag{3}$$

with G_I the mode I opening component, G_{II} the mode II opening component, G_{Ic} the mode I critical value, G_{IIc} the mode II critical value. The mode III component is neglected as the loading conditions are mainly defined in a 2 dimensional space.

2.4 Icing and testing process

The process used to create the ice samples is the same process described in [30]. The objective is to create many ice samples obtained in different icing conditions to study the ice properties of interest according to a wide range of ice densities.

The cold room enables lowering the ambient temperature down to -40°C and is equipped with an injection system allowing to create the icing conditions. The injection system is mounted on a rail fixed on the ceiling of the room. The water is injected at high pressure (70 bars) and pulverized into droplets of 320 microns median diameter using a spraying system with flat

jet nozzles. Droplets then fall toward the accretion area through gravity. The injected water is demineralized and stored in a cooling tank at low temperature just above freezing point ([0,1]°C) before injection.

The ice deposit realized in cold chamber is observed to be extremely uniform allowing accurate measurements of the thickness to give precise idea of the ice block volume (figure 2). The temperature range of the experiment was maximized to extend the validity of the study between -5.8°C and -24.2°C. The precipitation rate was in the range of 10 to 100 g/dm^2/h.

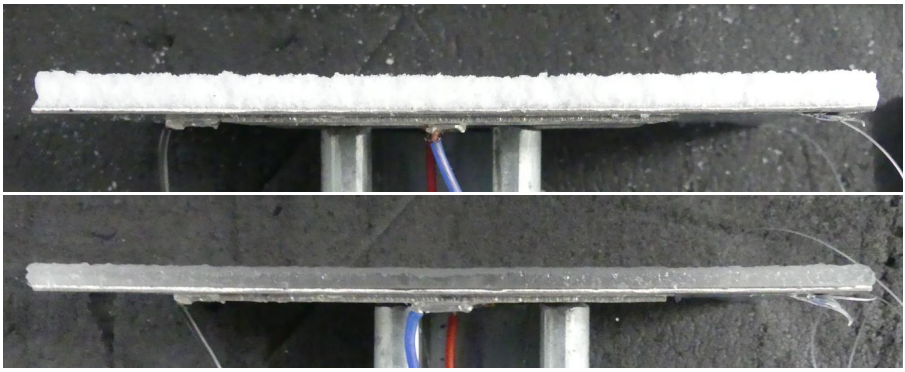

Fig. 2: Side view of two ice samples of different density highlighting the homogeneity of the ice layer thickness

More information on the icing process are available in [30].

2.5 Method for critical values estimation

An experimental set up is installed in the cold room enabling the mechanical loading of the samples and the measurement of the quantities of interest. The measurements and testing are therefore realized in the cold room enabling to keep the samples in the same confined cold environment from the ice accretion process to the end of the experiment. The samples are loaded by a piezo

ceramic actuator (PIC 181). The ceramic is excited using a sine-wave generator. The frequency of the sine-wave is swept on a given range to trigger the structure first eigenmode. A descending sweep is performed to ensure a good actuation of the mode at high vibrating magnitudes [52]. The structure is excited while being hold in "free" conditions by thin nylon strings. A mono-point laser vibrometer is used to measure the vibrating speed of the structure at its center (figure 3). The laser is surrounded by a heating box to ensure functioning at required temperature. An acquisition card PCI-6221 device is used to retrieve the signal from the laser. Upon fracture appearance, the stiffness of the structure drops and therefore, a drop in the mode frequency is observed. By monitoring this phenomenon, the method enables an accurate measurement of the vibration magnitude at the crack initiation. The data are filtered and displayed on a frequency chart enabling to retrieve the magnitude of the displacement corresponding to the crack appearance (figure 4).

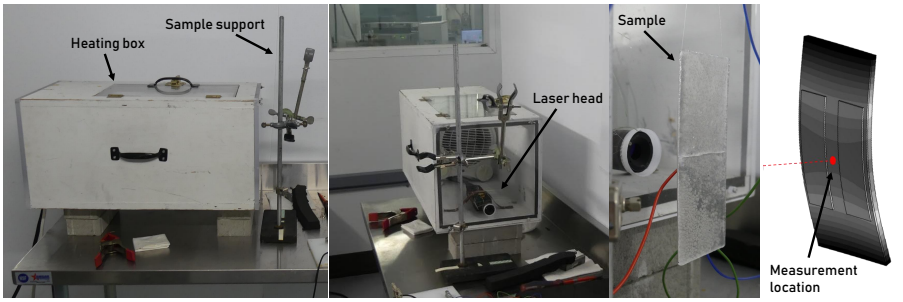

Fig. 3: Experimental set up for the measurement of the vibrating speed of the plate center

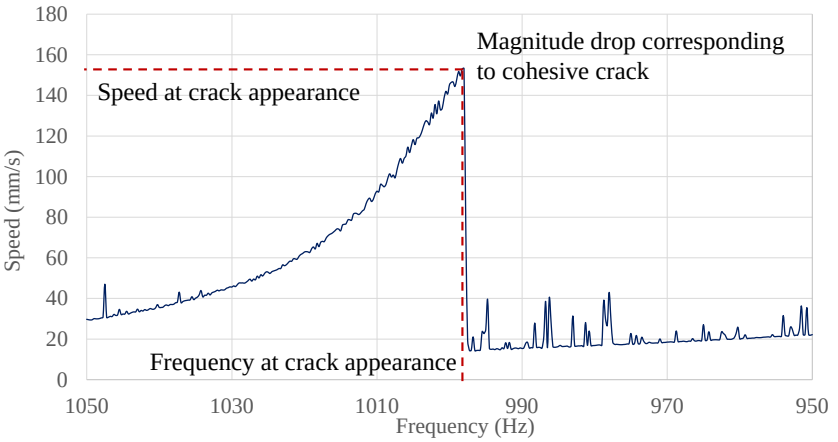

Fig. 4: Measurement of the speed of the sample center at breaking time

The magnitude of the displacement can be obtained from the speed of the point since the movement is sinusoidal (4).

$$\begin{aligned} \dot{x}(t) &= A\ cos(\omega t) \\ x(t) &= \frac{A}{\omega}\ sin(\omega t) \end{aligned} \tag{4}$$

with $\dot{x}$ the speed, A the magnitude of the speed, ω the angular frequency, x the displacement of the point and A/ω the magnitude of the displacement. As the estimation of the critical values is made thanks to the finite element model, the accuracy of the model is of utmost importance. A 3D finite element model of each substrate sample is realized using the FEM software ANSYS. Hexahedral elements are used to mesh the whole structure. The bodies are attached to the substrate using "bonded" contact function. As the sample are tested in free boundary conditions (held by nylon strings), no boundary conditions are given in the FEM analysis. The linear elasticity material properties used for the computations are given in Table 2. The ceramics properties are

defined as an-isotropic and taken from PI ceramic catalog (PIC 181). A preliminary study is realized to assess the validity of each sample model. The resonant frequencies of the first modes are computed through modal analysis for each of the bare (without ice) samples and compared with the experimental measured frequencies. The discrepancy of the numerical models is less than 2% for each sample, confirming their accuracy.

Table 2: Material properties

Material	Ti TA6V	Al 5754	Ice	PIC 181
Young's modulus (GPa)	110	71	Measured	-
Poisson's ratio	0.31	0.33	0.33	-
Density (kg/m^3)	4370	2770	Measured	7850

2.5.1 Critical tensile strength of ice

Ice layers are added to the 3D model. The ice is defined as a rectangular homogeneous and isotropic slab covering the whole surface. The density and the thickness measured experimentally are used to model the different ice layers for each test case. The Young's modulus is assessed using the formula given in [30].

$$E = E_0 \left[1.416 \left(\frac{\rho}{\rho_0} \right)^3 - 3.612\mathrm{e}^{-01} \left(\frac{\rho}{\rho_0} \right)^2 - 4.511\mathrm{e}^{-02} \left(\frac{\rho}{\rho_0} \right) \right] \tag{5}$$

with E_0 the Young's modulus with maximum density (9.0 GPa) and ρ_0 the density of pure ice (917 kg/m^3) [22, 27].

A modal analysis is ran to obtain the modal shape and stress field of the first eigenmode of the structure. Figure 5 shows an example of the modal stress field at the surface of the ice.

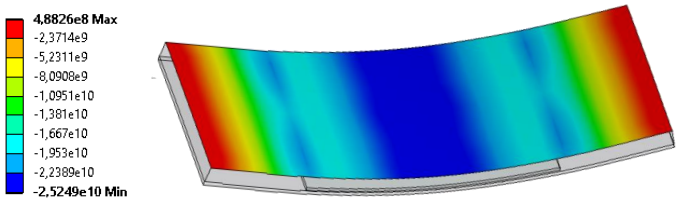

Fig. 5: Stress field at the surface of the ice for a given ice configuration under first mode of bending

Using the method described in [46, 53], the modal amplitude and stress field can be linearly re-scaled to the experimental values. For a given modal analysis, the displacement of the sample center x_{num} and the maximum principal stress on the ice σ_{Inum} are retrieved. Knowing the experimental displacement x_{exp} upon ice crack appearance, one can obtain the maximum principal stress σ_{Iexp} value:

$$\sigma_{Iexp} = \sigma_{Inum} \frac{x_{exp}}{x_{num}} \tag{6}$$

Based on the assumption on crack initiation made in section 2.3.1, the experimental stress obtained represents the maximum allowable tensile stress of the ice and therefore its tensile strength.

2.5.2 Critical fracture toughness of the ice

Following the ice fracture mechanisms described in [53, 54], after the full apparition of the cohesive crack, ice begins to debond adhesively. The adhesive crack extends outward from the cohesive crack location. The numerical model is modified by creating the cohesive crack and adding an adhesive crack of lengths ranging from 0 mm to 20 mm.

Based on the assumption on crack propagation made in section 2.3.2, the experimental energy release rate obtained represents the fracture toughness

of the ice. Figure 6 shows the mode shape of the 3D model representing the cracked configuration.

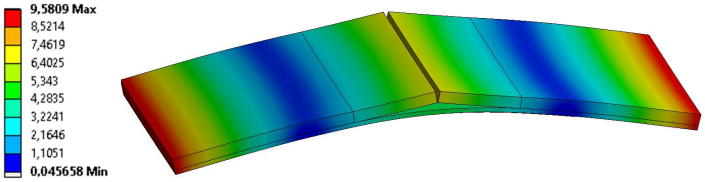

Fig. 6: Displacement field of the 3D model for energy release rate computation

Many methods exist to compute numerically the energy release rate. Computations are realized using ANSYS software in which a crack analysis tool is available. Using the crack tool, the stress intensity factors (SIF) and energy release rate around the crack tip can be retrieved using the VCCT (Virtual Crack Closure Technique) method and the J-integral method. Using the VCCT method or the SIF computation, one can assess the proportion of G_I and G_{II} [45, 55, 56]. Unfortunately, this fracture tool is not available for modal analysis.

A simplified model supporting the crack tool (static analysis) is therefore realized. The model is defined in 2D to enable finer meshing of the crack tip. The static model is assumed to be representative of the modal analysis as the crack propagation speed is much greater than the vibration speed of the plate, therefore, correspondence between mode shape and static deflection ensures an equivalence of the models. The similarity between the 2D model and previously defined 3D model is validated ensuring an equivalent strain energy arrangement and equivalent deflection of the beam under the artificial load used (Rayleigh hypothesis). The 2D half model is compounded of an ice layer, a substrate layer and a piezo layer. A pre-crack is defined at the ice substrate interface. As contact are not supported with the crack tool, the bodies are bonded sharing the interface nodes. A perfect clamp is imposed at the center

of the substrate as shown on figure 7.A linear quad mesh is used to match with fracture tool inquiries (figure 7). The mesh is mainly compounded of quad elements but triangles are use arround the crack tip location. The material properties remain the same as for the 3D model described above and are given in Table 2.

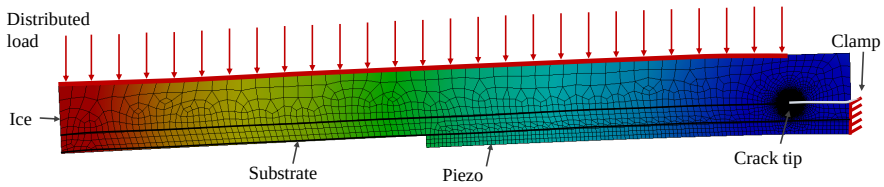

Fig. 7: 2D model definition

To assess the share between mode I and mode II openings in this case, the VCCT method is used. The G_{II}/G_I ratio is retrieved at the crack tip. The global G value is also retrieved using the J-integral method. Firstly, the study shows that whatever the length a of the crack, the opening mode is pure mode I opening. Hence, the G measured can be defined as G_I. The critical value computed using the method introduced in this article is therefore the critical energy release rate for mode opening G_{Ic}. Secondly, as the mode opening is computed to be pure mode I opening, the value considered for G is the value given by the J-integral method as it is less mesh dependent than the VCCT method, leading to more accurate computations [57].

As for cohesive crack appearance, a frequency shift is observed as the adhesive crack extends, which allows tracking the beginning of the crack propagation. For each configuration under study, the magnitude in the center of the sample x_{exp} and its corresponding crack length are measured. Then the vibration magnitude in the center of the sample x_{num} and the global energy release rate value G_{num} are computed from a modal analysis achieved for the

measured crack lengths. Finally, the energy release rate value estimated from experiment G_{exp} is retrieved from G_{num} and considering the square of the ratio of experimental and numerical displacements as explained in [46, 54]:

$$G_{exp} = G_{num} \frac{x_{exp}^2}{x_{num}^2} \tag{7}$$

3 Results

3.1 Cohesive strength of impact ice

A total of 43 samples are tested for measuring tensile strength for different ice densities. The method described in section 2.5.1 is used to retrieve the tensile strength upon cohesive crack appearance for each samples. For samples with high ice density, the cohesive crack appearance is identified both visually and by the magnitude drop on the frequency chart. However, for samples with lower ice density, the cracks are not always visible by sight as the ice is whiter and only the frequency chart is used to assess the appearance of cohesive cracks (Figure 8).

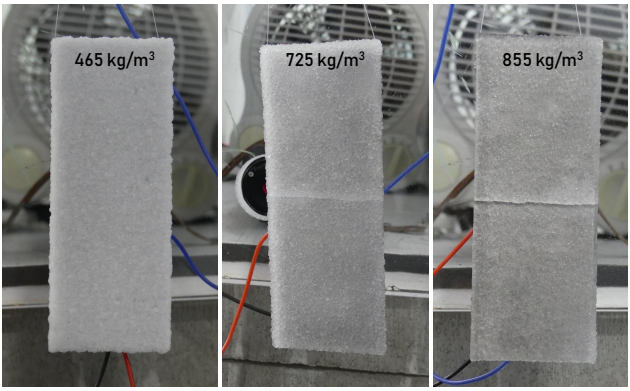

Fig. 8: Cohesive crack for ices of different densities, with invisible crack for low ice density

The value of the cohesive strength measured for each sample is plotted in function of the density on figure 9. From this study, the tensile strength of the ice appears to be highly correlated with its density. The tensile strength of the ice is decreasing as the ice gets more porous, which confirms the results obtained by Zong with a random pore model study [33].

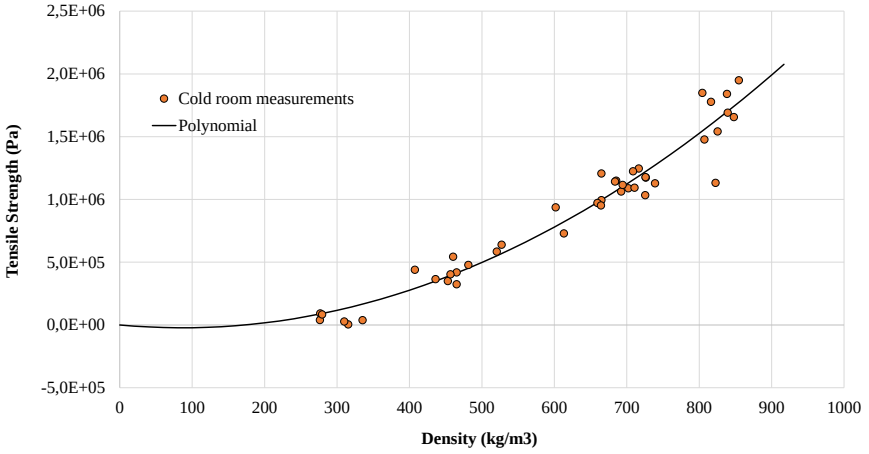

Fig. 9: Tensile strength of the ice in function of the density

From the data, a polynomial is computed to model the tensile strength versus the ice density. The range of the given model stops at the higher density obtained experimentally, i.e. 855 kg/m^3. However, if the polynomial is extrapolated to the maximum density, the maximum tensile strength σ_0 can be estimated to 2.07 MPa. Equation (8) gives the obtained expression of the tensile strength of ice according to its density for the [0 - 917 kg/m^3] range.

$$\sigma = \sigma_0 \left[1.232 \left(\frac{\rho}{\rho_0} \right)^2 - 0.232 \left(\frac{\rho}{\rho_0} \right) \right] \tag{8}$$

with σ the tensile strength of the ice, ρ its density [kg/m^3],and ρ_0 (917 kg/m^3) the pure ice density.

3.2 fracture toughness

As measuring the crack length is required to achieve the energy release rate computation, the samples with invisible cracks (low densities) are not suitable for the study. The number of samples usable for the G computation is hence reduced to 19. However, for a given sample, several lengths of adhesive cracks can be used to assess the energy release rate (figure 10).

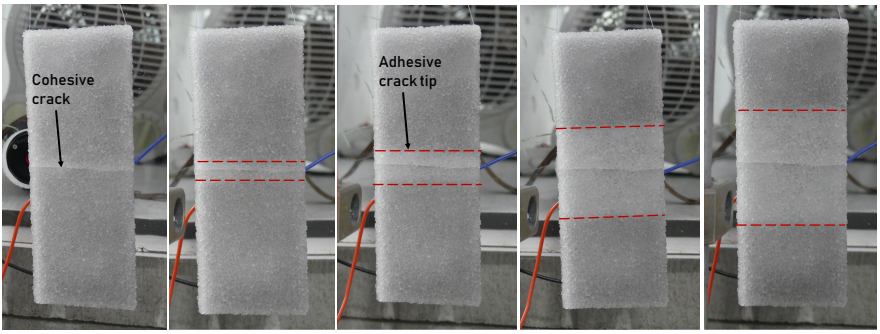

Fig. 10: Different adhesive propagation steps for a same sample of 725 kg/m^3 density

For each sample, the crack length is measured using a pixel measurement software. The G value is computed by using the J-integral method and retrieving the energy release rate for a crack corresponding to the experimental crack length (section 2.5.2). The first results of the study show that the measured G_c value tends to decrease as the crack extends (figure 11). As the crack grows, the frequency of the first mode of resonance of the modal analysis shows significant difference with the frequency measured experimentally, leading to an error between the model and the experiment. Figure 12 shows the Gc value computed according to the error between experimental and numerical frequencies. The domain of validity of the computation is therefore reduced to the measurements with a frequency error under 10%.

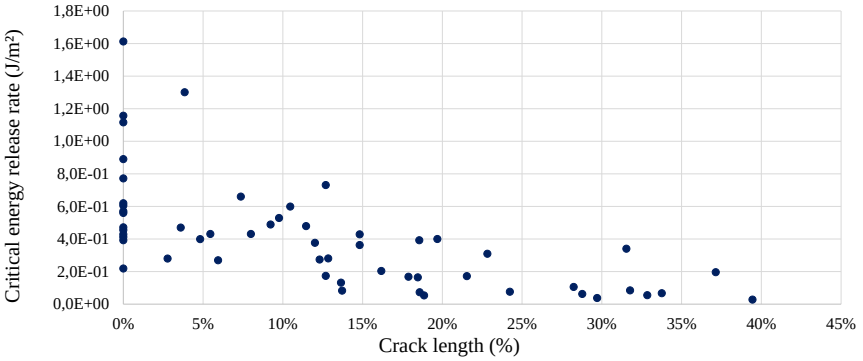

Fig. 11: G_c according to the crack length (% of the substrate length)

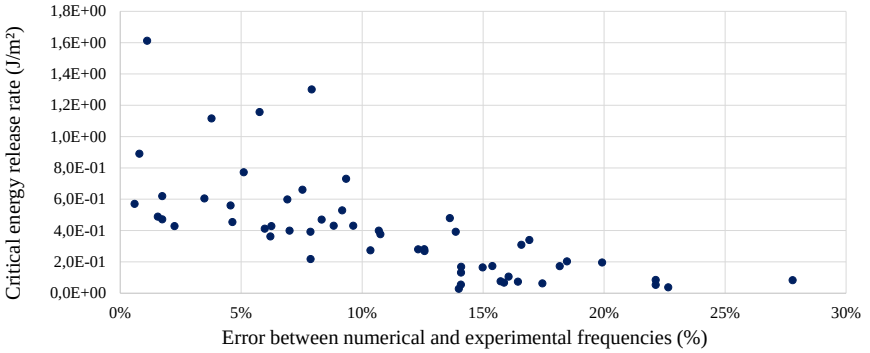

Fig. 12: G_c according to the numerical error of the model

Figure 13 shows the results from the usable data. The values present scattering but a decreasing trend in the G_{Ic} critical value is visible as the density increases, which was also observed by [42]. The use of aluminum or titanium material does not seem to have a particular influence on the critical value, which is probably due to the similar roughness (0.60 µm for titanium and 0.32µm for aluminum) of both substrates. Not taking highly scattered points into account (Figure 14), the trend of the G_c [J/m^2] value can be expressed by a linear function (9):

$$G_c = -9.546 \cdot 10^{-4}\ \rho + 1.249 \tag{9}$$

with ρ [kg/m^3] the density of the ice.

The definition of the trend is however highly limited by the reduced range of the density spectrum. On the interval, the G_c value could be considered constant. The average value for the data set is 0.55 J/m^2 with a standard deviation of 13% and a maximum deviation of 48%.

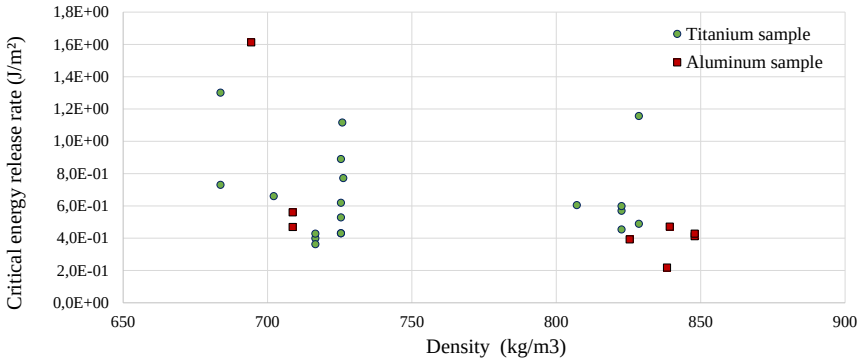

Fig. 13: G_c for both substrates according to the ice density

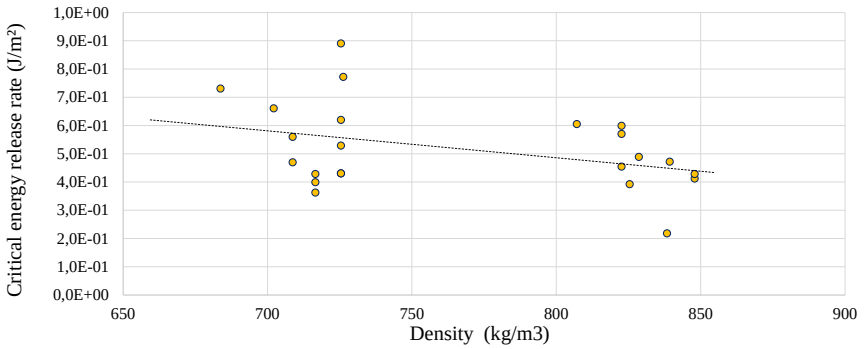

Fig. 14: G_c for both substrates according to the ice density without scattered data

4 Discussion

In the case of mechanical de-icing, the difficulty to initiate the crack can be assessed by the amount of strain required. The critical strain ϵ_c for cohesive fracture appearance can be computed from Hooke's law:

$$\epsilon_c = \frac{\sigma_c}{E} \tag{10}$$

with σ_c the tensile strength of the material and E the Young's modulus. In fact, if the strength decreases, the required strain is also decreasing. However, if the Young's modulus of the material decreases more than the strength (which is the case with the ice with a 3^{rd} order polynomial for Young's modulus and 2^{nd} order polynomial for cohesive strength), the required strain increases.

Making the assumption of a substrate highly stiffer than the ice, the strain in the ice can be considered as imposed by, and therefore equivalent to, the strain of the substrate. The critical strain of the ice is hence directly proportional to the deformation applied to the substrate. Using the expression of the ice Young's modulus E_{ice} given in [30], the critical elastic strain ϵ_c to reach the ice critical stress σ_c and thus initiate cohesive fractures can be computed with (10). By computing the critical strain required to initiate fracture according to the ice density, the deformation magnitude to be imposed to the structure can be directly assessed.

In the same way, the difficulty to propagate the crack can be estimated by the amount of strain required to reach G_c. The strain energy density W_{elas} can be defined as:

$$W_{elas} = \frac{1}{2} E \epsilon^2 \tag{11}$$

As the energy release rate is proportional to the strain energy [54]: $G \propto W_{elas}$, the critical strain for adhesive fracture propagation is proportional to the square root of G_c:

$$\epsilon_c \propto \sqrt{\frac{G_c}{E}} \tag{12}$$

Considering the ice of highest density as a reference (normalised density and normalised strain equal to 1), the following charts give the relative deformation and relative energy required to achieve cohesive failure (figure 15) and crack propagation for variable ice densities (figure 16).

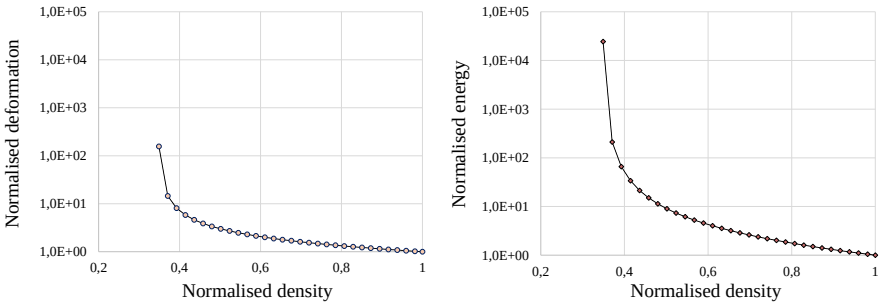

Fig. 15: Image of the deformation and energy magnitude required to initiate cohesive crack in the ice according to its normalised density

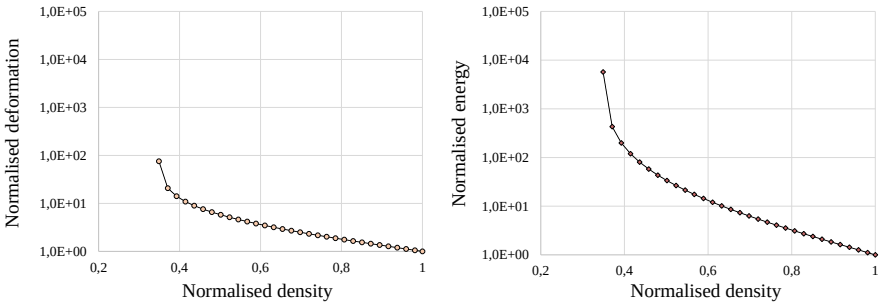

Fig. 16: Image of the deformation and energy magnitude required to propagate adhesive crack at the the ice/substrate interface according to the normalised density

The graphs show that as the density decreases, the deformation and energy must increase to initiate fractures. When reaching the critical porosity [30], the critical strain tends toward infinite value, showing that the mechanical removing of the ice would become impossible. However as the ice strength gets lower, it is probable that ice would shed under aerodynamic forces [58]. From these results, the ice appears to be more difficult to remove mechanically as the density gets lower. This conclusion suggests that the most critical icing conditions for mechanical de-icing system might be under light icing conditions leading to highly porous rime ice which would be harder to detach than glaze ice obtained under severe icing conditions. However, some studies on the ice adhesion properties [39, 42] highlighted the fact that porous ice tends to show cohesive fractures at the interface, which would lead to a different fracture mechanism. For such mechanism, the energy release rate computation proposed in this paper would be un-applicable.

In this study, the ice properties where studied using cold room ice deposits. However, in the case of aircraft icing, the ice is accreted at much higher speed, raising uncertainties about the applicability of the results on impact icing cases. The droplets impact regime can be studied by computing its Weber and Ohnesorge numbers [59]. In [30] the impact regime is computed for the cold room deposit and appears similar to most of the aircraft icing flight conditions, encouraging the authors in thinking that the models obtained could be suitable for aircraft impact ice.

5 Conclusion

An hybrid experimental/numerical method has been developed to assess some of the key mechanical properties of atmospheric ice. The proposed method

appears to be efficient for the accurate measurement of the mechanical properties of ice thanks to its high strain rate and has shown remarkable repeatability for ice measurements. Using a cold room, many icing conditions (temperature, precipitation rate) were generated, leading to the formation of a large variety of ice samples, characterized by the ice density. The results of this study have demonstrated that the tensile strength of ice can be defined as a function of ice density alone as same results where obtained for ice of similar density, grown in different icing conditions. An expression of the tensile strength based on the interpolation of experimental results is established and given according to the density. The fracture toughness of the ice is also investigated according to ice density. Due to the reduced range of density analyzed for this parameter, the trend of the critical energy release rate over the full density range is hard to assess. However, a range of values is given for ice of high density. Finally, the conditions to achieve mechanical de-icing are discussed. Using the results from the first part of the study [30], the deformation and energy magnitudes required to initiate or propagate cracks are compared according to the density of the ice. As the density decreases, the critical strain for both initiation and propagation increases. In the case of fracture initiation, the Young's modulus decreases faster than the tensile strength leading to increase of the critical strain with porosity. As G_c increases with porosity, critical strain gets higher, making the ice more difficult to crack and detach for low densities.

References

[1] Gent, R.W., Dart, N.P., Cansdale, J.T.: Aircraft icing. Philosophical Transactions of the Royal Society of London. Series A: Mathematical, Physical and Engineering Sciences **358**(1776), 2873–2911 (2000)

[2] Pouryoussefi, S.G., Mirzaei, M., Nazemi, M.-M., Fouladi, M., Doostmahmoudi, A.: Experimental study of ice accretion effects on aerodynamic performance of an naca 23012 airfoil. Chinese Journal of Aeronautics **29**(3), 585–595 (2016). https://doi.org/10.1016/j.cja.2016.03.002

[3] Shin, J., BOND, T.: Results of an icing test on a naca 0012 airfoil in the nasa lewis icing research tunnel. In: 30th Aerospace Sciences Meeting and Exhibit, p. 647 (1992)

[4] Etemaddar, M., Hansen, M.O.L., Moan, T.: Wind turbine aerodynamic response under atmospheric icing conditions. Wind Energy **17**(2), 241–265 (2014)

[5] Cao, Y., Chen, K.: Helicopter icing. The Aeronautical Journal **114**(1152), 83–90 (2010)

[6] Samad, A., Villeneuve, E., Blackburn, C., Morency, F., Volat, C.: An experimental investigation of the convective heat transfer on a small helicopter rotor with anti-icing and de-icing test setups. Aerospace **8** (2021). https://doi.org/10.3390/aerospace8040096

[7] Villeneuve, E., Blackburn, C., Volat, C.: Design and development of an experimental setup of electrically powered spinning rotor blades in icing wind tunnel and preliminary testing with surface coatings as hybrid protection solution. Aerospace **8**, 98 (2021). https://doi.org/10.3390/aerospace8040098

[8] Laforte, J.L., Allaire, M.A., Laflamme, J.: State-of-the-art on power line de-icing. Atmospheric Research **46**(1), 143–158 (1998). https://doi.org/10.1016/S0169-8095(97)00057-4

[9] Villeneuve, E., Harvey, D., Zimcik, D., Aubert, R., Perron, J.: Piezoelectric deicing system for rotorcraft. Journal of the American Helicopter Society **60**(4), 1–12 (2015)

[10] Villeneuve, E., Volat, C., Ghinet, S.: Numerical and experimental investigation of the design of a piezoelectric de-icing system for small rotorcraft part 1/3: Development of a flat plate numerical model with experimental validation. Aerospace **7**(5), 62 (2020)

[11] Villeneuve, E., Volat, C., Ghinet, S.: Numerical and experimental investigation of the design of a piezoelectric de-icing system for small rotorcraft part 2/3: Investigation of transient vibration during frequency sweeps and optimal piezoelectric actuator excitation. Aerospace **7**(5), 49 (2020)

[12] Villeneuve, E., Volat, C., Ghinet, S.: Numerical and experimental investigation of the design of a piezoelectric de-icing system for small rotorcraft part 3/3: Numerical model and experimental validation of vibration-based de-icing of a flat plate structure. Aerospace **7**(5), 54 (2020)

[13] Ramanathan, S., Varadan, V.V., Varadan, V.K.: Deicing of helicopter blades using piezoelectric actuators. In: Smart Structures and Materials 2000: Smart Electronics and MEMS, vol. 3990, pp. 281–293 (2000). https://doi.org/10.1117/12.388906. International Society for Optics and Photonics. https://www.spiedigitallibrary.org/conference-proceedings-of-spie/3990/0000/Deicing-of-helicopter-blades-using-piezoelectric-actuators/10.1117/12.388906.short?SSO=1

[14] Lin, Y., Venna, S.V.: Inflight deicing of self-actuating aircraft wing

structures with piezoelectric actuators. In: ASME 2002 International Mechanical Engineering Congress and Exposition, pp. 243–247 (2002). American Society of Mechanical Engineers. https://proceedings.asmedigitalcollection.asme.org/proceeding.aspx?articleid=1580344

[15] Pommier-Budinger, V., Budinger, M., Rouset, P., Dezitter, F., Huet, F., Wetterwald, M., Bonaccurso, E.: Electromechanical Resonant Ice Protection Systems: Initiation of Fractures with Piezoelectric Actuators. AIAA Journal **56**(11), 4400–4411 (2018). https://doi.org/10.2514/1.J056662. Accessed 2020-05-06

[16] Labeas, G.N., Diamantakos, I.D., Sunaric, M.M.: Simulation of the electroimpulse de-icing process of aircraft wings. Journal of Aircraft **43**(6), 1876–1885 (2006)

[17] Endres, M., Sommerwerk, H., Mendig, C., Sinapius, M., Horst, P.: Experimental study of two electro-mechanical de-icing systems applied on a wing section tested in an icing wind tunnel. CEAS Aeronautical Journal **8**(3), 429–439 (2017)

[18] Villeneuve, E., Ghinet, S., Volat, C.: Experimental study of a piezoelectric de-icing system implemented to rotorcraft blades. Applied Sciences **11**, 9869 (2021). https://doi.org/10.3390/app11219869

[19] Villeneuve, E., Ghinet, S., Volat, C.: Experimental study of a piezoelectric de-icing system implemented to rotorcraft blades. Applied Sciences **11**(21) (2021). https://doi.org/10.3390/app11219869

[20] Hobbs, P.V.: Ice Physics (2010). Google-Books-ID: 7Is6AwAAQBAJ

[21] Fletcher, N.H.: Mechanical properties. Cambridge Monographs on

Physics, pp. 165–197. Cambridge University Press, ??? (1970). https://doi.org/10.1017/CBO9780511735639.010

[22] Mellor, M.: Mechanical properties of polycrystalline ice, 217–245 (1980)

[23] Dorsey, N.E., et al.: Properties of ordinary water-substance in all its phases (1940)

[24] Northwood, T.: Sonic determination of the elastic properties of ice. Canadian Journal of Research **25**(2), 88–95 (1947)

[25] Gold, L.W.: Some observations on the dependence of strain on stress for ice. Canadian Journal of Physics **36**(10), 1265–1275 (1958) https://arxiv.org/abs/https://doi.org/10.1139/p58-131. https://doi.org/10.1139/p58-131

[26] Gold, L., Sinha, N.: The rheological behaviour of ice at small strains, 117–128 (1980)

[27] Schulson, E.M.: The structure and mechanical behavior of ice. Jom **51**(2), 21–27 (1999)

[28] Nakaya, U., et al.: Visco-elastic properties of processed snow (1959)

[29] Gammon, P.H., Kiefte, H., Clouter, M.J., Denner, W.W.: Elastic constants of artificial and natural ice samples by brillouin spectroscopy. Journal of Glaciology **29**(103), 433–460 (1983). https://doi.org/10.3189/S0022143000030355

[30] Palanque, V., E.Villeneuve, M.Budinger, V.Budinger, G.Momen: Experimental measurement and expression of atmospheric ice young's modulus

according to its density. Submitted to Cold Region science and technologies (2022)

[31] Frankenstein, G.E., Garner, R.: Dynamic young's modulus and flexural strength of sea ice **222** (1970)

[32] Georges, D., Saletti, D., Montagnat, M., Forquin, P., Hagenmuller, P.: Influence of porosity on ice dynamic tensile behavior as assessed by spalling tests. Journal of Dynamic Behavior of Materials **7**(4), 575–590 (2021)

[33] Zong, Z.: A random pore model of sea ice for predicting its mechanical properties. Cold Regions Science and Technology **195**, 103473 (2022). https://doi.org/10.1016/j.coldregions.2021.103473

[34] Druez, J., Nguyen, D.D., Lavoie, Y.: Mechanical properties of atmospheric ice. Cold Regions Science and Technology **13**(1), 67–74 (1986). https://doi.org/10.1016/0165-232X(86)90008-X

[35] Druez, J., McComber, P., Tremblay, C.: Experimental results on the tensile strength of atmospheric ice. Transactions of the Canadian society for mechanical engineering **13**(3), 59–64 (1989)

[36] Petrovic, J., Vasudevan, A.: Key developments in high temperature structural silicides. Materials Science and Engineering: A **261**(1-2), 1–5 (1999)

[37] Golovin, K., Dhyani, A., Thouless, M., Tuteja, A.: Low–interfacial toughness materials for effective large-scale deicing. Science **364**(6438), 371–375 (2019)

[38] Work, A., Lian, Y.: A critical review of the measurement of ice adhesion to solid substrates. Progress in Aerospace Sciences **98**, 1–26 (2018)

[39] Rønneberg, S., Laforte, C., Volat, C., He, J., Zhang, Z.: The effect of ice type on ice adhesion. AIP advances **9**(5), 055304 (2019)

[40] Scavuzzo, R., Chu, M.L.: Structural properties of impact ices accreted on aircraft structures. Technical report (1987)

[41] Raraty, L., Tabor, D.: The adhesion and strength properties of ice. Proceedings of the Royal Society of London. Series A. Mathematical and Physical Sciences **245**(1241), 184–201 (1958)

[42] Pervier, M.A., Hammond, D.W.: Measurement of the fracture energy in mode i of atmospheric ice accreted on different materials using a blister test. Engineering Fracture Mechanics **214**, 223–232 (2019). https://doi.org/10.1016/j.engfracmech.2019.02.003

[43] Yeong, Y.H., Milionis, A., Loth, E., Sokhey, J., Lambourne, A.: Atmospheric ice adhesion on water-repellent coatings: Wetting and surface topology effects. Langmuir **31**(48), 13107–13116 (2015) https://arxiv.org/abs/https://doi.org/10.1021/acs.langmuir.5b02725. https://doi.org/10.1021/acs.langmuir.5b02725. PMID: 26566168

[44] Andrews, E., Majid, H., Lockington, N.: Adhesion of ice to a flexible substrate. Journal of materials science **19**(1), 73–81 (1984)

[45] Huré, M., Olivier, P., Garcia, J.: Effect of cassie-baxter versus wenzel states on ice adhesion: A fracture toughness approach. Cold Regions Science and Technology **194**, 103440 (2022)

[46] Palanque, V., Budinger, M., Pommier-Budinger, V., Bennani, L., Delsart, D.: Electro-mechanical Resonant Ice Protection Systems: Power requirements for fractures initiation and propagation. In: AIAA AVIATION 2021 FORUM. AIAA AVIATION Forum. American Institute of Aeronautics and Astronautics, ??? (2021). https://doi.org/10.2514/6.2021-2651. https://arc.aiaa.org/doi/10.2514/6.2021-2651 Accessed 2021-08-02

[47] G.Gastaldo, V.Palanque, M.Budinger, V.Pommier-Budinger: Stress and energy release rate influence on ice shedding with resonant electromechanical de-icing systems. ICAS Conference (2022)

[48] Tryde, P. (ed.): Physics and Mechanics of Ice: Symposium Copenhagen, August 6–10, 1979, Technical University of Denmark. Springer, Berlin, Heidelberg (1980). https://doi.org/10.1007/978-3-642-81434-1. http://link.springer.com/10.1007/978-3-642-81434-1 Accessed 2020-05-06

[49] Zehnder, A.T.: In: Wang, Q.J., Chung, Y.-W. (eds.) Griffith Theory of Fracture, pp. 1570–1573. Springer, Boston, MA (2013). https://doi.org/10.1007/978-0-387-92897-5_259. https://doi.org/10.1007/978-0-387-92897-5_259

[50] Hutchinson, J.W., Suo, Z.: Mixed mode cracking in layered materials. In: Advances in Applied Mechanics vol. 29, pp. 63–191. Elsevier, ??? (1991)

[51] Reeder, J.: An evaluation of mixed-mode delamination failure criteria. Technical report (1992)

[52] Davis, W.O.: Measuring quality factor from a nonlinear frequency response with jump discontinuities. Journal of Microelectromechanical Systems **20**(4), 968–975 (2011). https://doi.org/10.1109/JMEMS.2011.2159103

[53] Budinger, M., Pommier-Budinger, V., Bennani, L., Rouset, P., Bonaccurso, E., Dezitter, F.: Electromechanical Resonant Ice Protection Systems: Analysis of Fracture Propagation Mechanisms. AIAA Journal **56**(11), 4412–4422 (2018). https://doi.org/10.2514/1.J056663. Accessed 2020-05-06

[54] Budinger, M., Pommier-Budinger, V., Reysset, A., Palanque, V.: Electromechanical resonant ice protection systems: Energetic and power considerations. AIAA Journal **59**(7), 2590–2602 (2021) https://arxiv.org/abs/https://doi.org/10.2514/1.J060008. https://doi.org/10.2514/1.J060008

[55] Begley, J., Landes, J.: The j integral as a fracture criterion (1972)

[56] Rice, J.R., Suo, Z., Wang, J.-S., *et al.*: Mechanics and thermodynamics of brittle interfacial failure in bimaterial systems. Acta-Scripta Metallurgica Proceedings Series **4**, 269–294 (1990)

[57] Nor, K.M., Ibrahim, M.N., Choiron, M.A.: An overview of fracture mechanics with ansys. Mechanical Engineering **10**(5), 59–67 (2018)

[58] Bennani, L., Villedieu, P., Salaun, M.: A mixed adhesion–brittle fracture model and its application to the numerical study of ice shedding mechanisms. Engineering Fracture Mechanics **158**, 59–80 (2016). https://doi.org/10.1016/j.engfracmech.2016.02.050

[59] Garcia, N., Villedieu, P., Dewitte, J., Lavergne, G.: A new droplet-wall interaction model. (2008)